insulin carbonyl carbon in the insulin-trehalose system is longer than in the insulin-dextran system, indicating that the molecular mobility of insulin is decreased by trehalose, since longer $T_{1\rho}$ indicates slower motion in the slow motional regime (Fig. 3).

Retardation of spin-lattice relaxation of protein carbonyl carbon brought about by the addition of sugars is also observed for the carbonyl carbon of β-galactosidase freeze-dried with sucrose, trehalose, or stachyose, as shown in Figure 11 (33). The molecular mobility of the protein is most effectively decreased by sucrose.

The T_1 and $T_{1\rho}$ of protein carbonyl carbon described above represent the average of T_1 and $T_{1\rho}$ for multiple carbonyl carbons present in the protein molecule. More detailed site-specific analysis becomes possible by the ^{13}C-labeling of an amino acid at a specific site of interest.

Laboratory and Rotating Frame Spin-Lattice Relaxation Times of Fluorine

^{19}F-NMR has high sensitivity and specificity and has been used to determine the molecular mobility of ^{19}F-labeled proteins (34) as well as small molecules containing ^{19}F (35). Figure 12 shows the temperature dependence of T_1 and $T_{1\rho}$ of

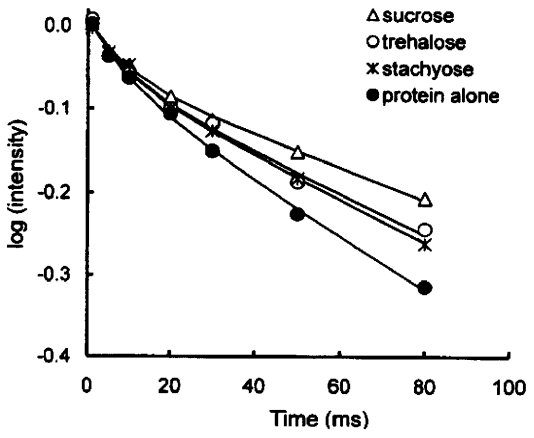

FIGURE 11 Time course of spin-lattice relaxation for carbonyl carbon of β-galactosidase freeze-dried with sucrose, trehalose, or stachyose at 25°C and 12% RH.

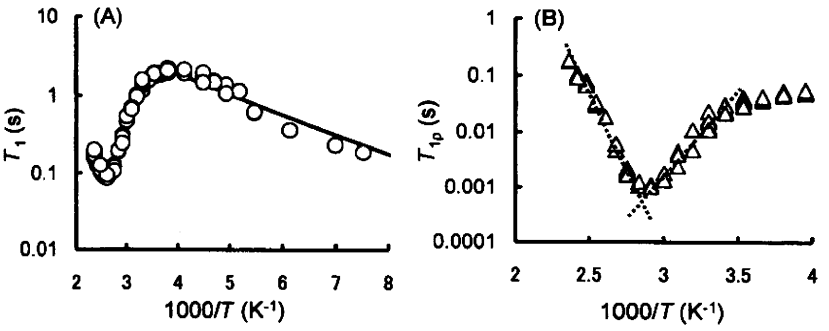

FIGURE 12 Temperature dependence of T_1 (**A**) and $T_{1\rho}$ (**B**) of flufenamic acid ^{19}F in solid dispersions with PVP. *Abbreviation*: PVP, polyvinylpyrrolidone.

^{19}F in amorphous flufenamic acid dispersed with PVP (drug-PVP, 7:3). The T_1 of ^{19}F shows a minimum at approximately 110°C as well as a maximum at approximately −10°C, as shown in Figure 12A. The temperature dependence can be described by assuming that the ^{19}F atom has two Arrhenius-type motions with an equivalent contribution to the process of T_1 but with different activation energies of 50 and 5 kJ/mol, as shown by the solid line in Figure 12A. The motion with greater activation energy may be attributed to β-relaxation and the other one to the rotation of the trifluoromethyl group, which is faster than β-relaxation.

The $T_{1\rho}$ of ^{19}F in flufenamic acid shows a minimum at approximately 60°C, as shown in Figure 12B. The temperature coefficient of $T_{1\rho}$ is about 50 kJ/mol at temperatures below 60°C, suggesting that $T_{1\rho}$ is determined by β-relaxation in this temperature range. In contrast, a greater temperature coefficient of $T_{1\rho}$ is observed at temperatures above 60°C, suggesting that $T_{1\rho}$ is determined by a larger-scale motion than β-relaxation. Thus, motion reflected by the T_1 and $T_{1\rho}$ of ^{19}F varies with temperature.

RELATIONSHIP BETWEEN STORAGE STABILITY AND MOLECULAR MOBILITY AS DETERMINED BY NMR RELAXATION TIMES

The storage stability of pharmaceuticals in the solid state is largely affected by molecular mobility. Changes in the molecular mobility of amorphous pharmaceuticals at T_g bring about changes in the temperature dependence of chemical and physical degradation rates. Coupling between chemical degradation and molecular mobility has been reported for several drugs of small molecular weight in freeze-dried formulation (1–5); hydrolysis of aspirin in freeze-dried hydroxypropyl-β-cyclodextrin/aspirin complex (1), hydrolysis of peptides in freeze-dried formulations containing cross-linked sucrose polymer (3), and deamidation of peptide in freeze-dried formulations containing poly(vinylpyrrolidone) (4,5). In addition to chemical instability, physical instability of pharmaceuticals, such as crystallization of amorphous compounds, is related to molecular mobility (36–40). Crystallization of freeze-dried sucrose is inhibited in the presence of PVP at a level as low as 10% due to the decreased molecular mobility of sucrose as indicated by the decreased enthalpy relaxation of the mixtures relative to sucrose alone (41).

Coupling between degradation and molecular mobility has also been reported for degradation of protein pharmaceuticals (6–15). An excellent correlation has been demonstrated between T_g and chemical degradation of freeze-dried antibody-vinca conjugate (8).

This section discusses the relationship between the storage stability of freeze-dried formulations and the molecular mobility as determined by NMR relaxation times, described in the previous section. Focus is placed on the degradation of small molecular weight drugs via bimolecular reaction and protein aggregation in the freeze-dried formulations.

Correlations Between Storage Stability and Structural Relaxation as Reflected by NMR Relaxation Times

NMR relaxation times are useful to determine fast dynamics of freeze-dried formulations, whereas structural relaxation of freeze-dried formulations, which

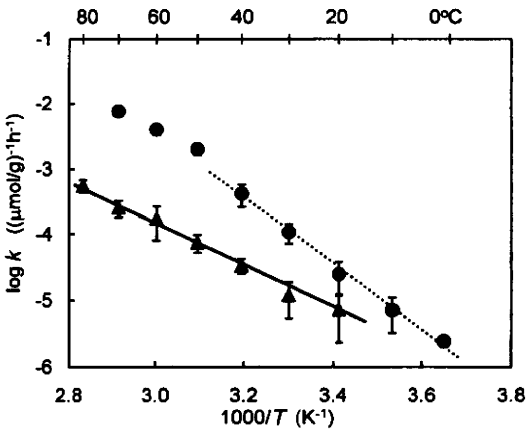

FIGURE 13 Temperature dependence of acetyl transfer between aspirin and sulfadiazine in freeze-dried formulations containing dextran at 12% (▲) and 60% RH (●).

is global mobility rapidly enhanced at temperatures above T_g, is also reflected by NMR relaxation times. Correlations between storage stability and structural relaxation as reflected by NMR relaxation times have been demonstrated for various freeze-dried formulations. Figure 13 shows the temperature dependence of the rate constant for acetyl transfer between aspirin and sulfadiazine in freeze-dried formulations containing dextran. Acetyl transfer is a bimolecular reaction in which the translational diffusion of reactant molecules becomes rate determining when molecular mobility is limited in the solid state (42). The rate constant of acetyl transfer (k_T) and the pseudo rate constant of hydrolysis ($k_{H,pseudo}$) that occurs in parallel with acetyl transfer in the presence of water are described by following equations.

$$\frac{d[SD]}{dt} = -k_T[SD][ASA] \tag{10}$$

$$\frac{d[ASA]}{dt} = -k_T[SD][ASA] - k_{H,pseudo}[ASA] \tag{11}$$

The temperature dependence of acetyl transfer at 60% RH exhibits a distinct break at approximately 40°C, although it is linear at 12% RH. The temperature of this distinct break observed at 60% RH is coincident with the T_{mc} as determined by the spin-spin relaxation measurements described in section "Molecular Mobility as Determined by NMR Relaxation Times." This indicates that the rate of acetyl transfer is affected by a change in the translational mobility of aspirin and sulfadiazine molecules at T_{mc}, resulting in a change in temperature dependence. The temperature dependence of acetyl transfer at 12% RH does not show any break because T_{mc} at 12% RH is higher than the highest temperature for the measurement. Compared with acetyl transfer, hydrolysis of aspirin occurring in parallel with acetyl transfer does not show such a distinct break at T_{mc}, even though hydrolysis is also a bimolecular reaction.

Similarly, no distinct break was observed in the temperature dependence of hydrolysis of cephalothin in freeze-dried formulations containing dextran, as shown in Figure 14. The hydrolysis rate of cephalothin increased with increasing humidity because the rate-limiting step involves water as a reactant. The

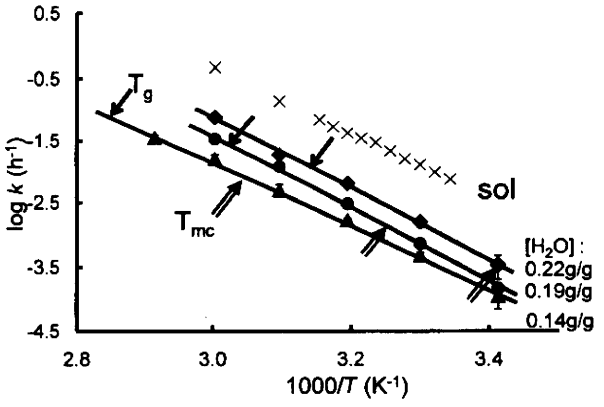

FIGURE 14 Temperature dependence of cephalothin hydrolysis in freeze-dried formulation containing dextran at 23% (▲), 60% (●), and 75% RH (◆).

temperature dependence of the apparent first-order rate constant is linear at all humidities in a manner similar to that of hydrolysis in aqueous solution, regardless of their T_{mc} indicated by arrows in the figure. The temperature dependence is also unaffected by the T_g of the formulations that are approximately 20°C higher than the T_{mc}. Since the translational mobility of drug and water molecules in freeze-dried formulations is affected by T_g and/or T_{mc}, the hydrolysis rate should be affected by T_g and/or T_{mc} if the translational diffusion of the drug and/or water molecules is rate limiting. The absence of a break in temperature dependence around T_g and T_{mc} suggests that the translational diffusion is not rate limiting. Since the translational diffusion of water can be considered to be much faster than that of the larger cephalothin molecule, the diffusion barrier of water molecules may be smaller than the chemical activational barrier. This interpretation is supported by the finding that the activation energy for the hydrolysis of cephalothin in the freeze-dried formulations containing dextran (between 23 and 26 kcal/mol) is close to the apparent activation energy obtained for hydrolysis in solution (24 kcal/mol). Because of the small diffusion barrier of water in freeze-dried formulations compared to the activational barrier, the hydrolysis rate of cephalothin is not affected by T_g and/or T_{mc}, even if the translational mobility of water molecules changes around T_g and/or T_{mc}.

Correlations Between Storage Stability and Fast Dynamics as Determined by NMR Relaxation Times

Protein aggregation, one of the most common degradation pathways of freeze-dried protein formulations, also appears to be closely related to the structural relaxation as reflected by NMR relaxation times. Figure 15 shows the temperature dependence of the time required for 10% protein aggregation (t_{90}) in freeze-dried β-galactosidase formulation containing methylcellulose (43). At 60% RH, the slope changes around the T_g measured by NMR (T_{mc}). No change in temperature dependence of t_{90} is observed at 12% RH, at which the T_{mc} is higher than the highest temperature for the measurement.

Apparent correlation between protein aggregation rate and structural relaxation is also observed for β-galactosidase freeze-dried with sugars. As shown in Figure 16, the slope of $t_{90} - T_g/T$ plots changes at around T_g, suggesting that aggregation rate is related to structural relaxation (33). However,

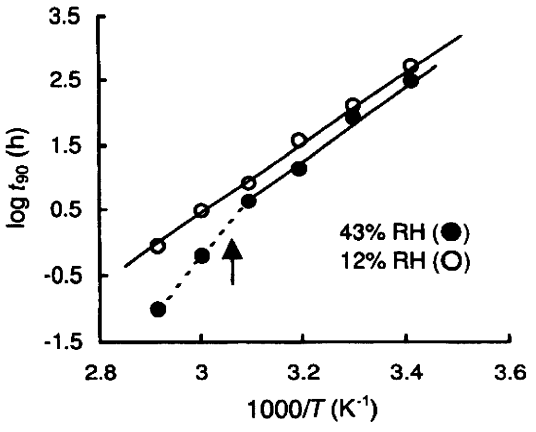

FIGURE 15 Temperature dependence of t_{90} for β-galactosidase aggregation in freeze-dried formulation containing methylcellulose.

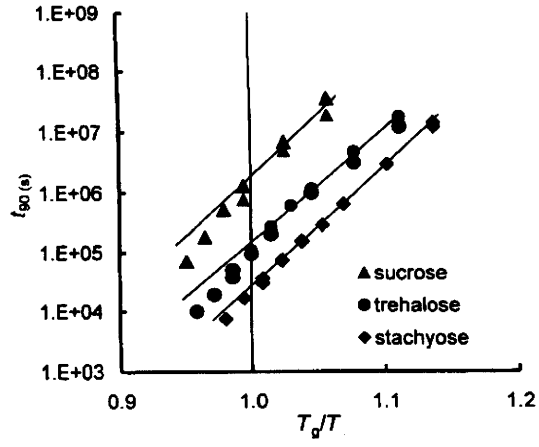

FIGURE 16 t_{90} for β-galactosidase aggregation in freeze-dried formulation containing sucrose, trehalose, or stachyose plotted against T_g/T.

structural relaxation cannot be considered to be the most relevant motion to the protein degradation, because sucrose, which has the shortest structural relaxation time, stabilizes the protein most effectively. These findings suggest that molecular motion other than structural relaxation contributes to the protein degradation. As shown in Figure 11, the $T_{1\rho}$ process of the protein carbonyl carbon is retarded by the addition of sugars, indicating that the fast dynamics of the protein is decreased by sugars. Sucrose is most effective in decreasing the protein dynamics. This suggests that the aggregation rate of β-galactosidase is correlated to the fast dynamics of the protein as determined by NMR relaxation times.

Figure 17 shows the temperature dependence of t_{90} observed for the degradation of insulin freeze-dried with trehalose or PVP (44). For insulin freeze-dried with trehalose stored at 12% RH, the slope of $t_{90} - T_g/T$ plot changed at around T_g, suggesting that degradation rate of insulin is correlated with structural relaxation. In contrast, for insulin freeze-dried with PVP, $t_{90} - T_g/T$ plots are linear at temperatures around T_g without a change in the slope. The value of t_{90} at T_g varies with humidity, indicating that structural relaxation is not the major factor that determines the degradation rate of insulin. If the

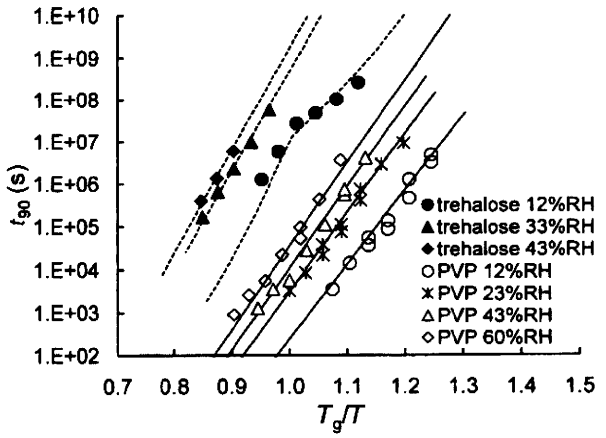

FIGURE 17 t_{90} for insulin degradation in freeze-dried formulation containing trehalose or PVP plotted against T_g/T.

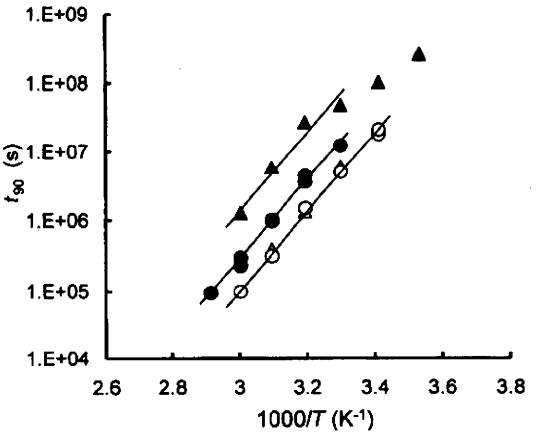

FIGURE 18 Temperature dependence of t_{90} for insulin degradation in freeze-dried formulation containing trehalose or dextran. ●, dextran 12% RH; ○, dextran 43% RH; ▲, trehalose 12% RH; △, trehalose 43% RH.

degradation rate is determined only by structural relaxation, t_{90} at T_g should not vary with humidity, because structural relaxation time is constant (100 seconds) at T_g regardless of humidity. These findings suggest that molecular motion other than structural relaxation contributes the insulin degradation, as suggested for the aggregation of β-galactosidase freeze-dried with sugars.

As shown in Figure 18, the t_{90} for the degradation of insulin freeze-dried with dextran is shorter than that of insulin freeze-dried with trehalose at 12% RH, and this difference in t_{90} is eliminated at 43% RH (32). As shown in Figure 10, the molecular mobility of the carbonyl carbon of insulin freeze-dried with trehalose, as determined by $T_{1\rho}$, is lower than that of insulin freeze-dried with dextran, as described in the section "Molecular Mobility as Determined by NMR Relaxation Times." This difference in mobility is eliminated at 43% RH, similar to the difference in t_{90}. These findings suggest that trehalose decreases the mobility of insulin in low humidity condition, and this decrease in mobility is related to the increase in insulin stability. Thus, the degradation rate of insulin also appears to be correlated to fast dynamics as determined by NMR relaxation times.

REFERENCES

1. Duddu SP, Weller K. Importance of glass transition temperature in accelerated stability testing of amorphous solids: case study using a lyophilized aspirin formulation. J Pharm Sci 1996; 85:345–347.
2. Herman BD, Sinclair BD, Milton N, et al. The effect of bulking agent on the solid-state stability of freeze-dried methylprednisolone sodium succinate. Pharm Res 1994; 11:1467–1473.
3. Streefland L, Auffret AD, Franks F. Bond cleavage reactions in solid aqueous carbohydrate solutions. Pharm Res 1998; 15:843–849.
4. Lai MC, Hageman MJ, Schowen RL, et al. Chemical stability of peptides in polymers. 1: Effect of water on peptide deamidation in poly(vinyl alcohol) and poly(vinyl pyrrolidone) matrixes. J Pharm Sci 1999; 88:1073–1080.
5. Lai MC, Hageman MJ, Schowen RL, et al. Chemical stability of peptides in polymers. 2. Discriminating between solvent and plasticizing effects of water on peptide deamidatin in poly(vinylpyrrolidone). J Pharm Sci 1999; 88:1081–1089.
6. Duddu SP, Zhang G, Dal Monte PR. The relationship between protein aggregation and molecular mobility below the glass transition temperature of lyophilized formulations containing a monoclonal antibody. Pharm Res 1997; 14:596–600.
7. Pikal MJ, Dellerman K, Roy ML. Formulation and stability of freeze-dried proteins: effects of moisture and oxygen on the stability of freeze-dried formulations of human growth hormone. Dev Biol Stand 1991; 74:21–38.
8. Roy ML, Pikal MJ, Rickard EC, et al. The effects of formulation and moisture on the stability of a freeze-dried monoclonal antibody-vinca conjugate: a test of the WLF glass transition theory. Dev Biol Stand 1991; 74:323–340.
9. Hageman M. Water sorption and solid-state stability of proteins. In: Ahern TJ, Manning MC, eds. Stability of Protein Pharmaceuticals. Part A: Chemical and Physical Pathways of Protein Degradation. New York: Plenum Press, 1992.
10. Bell LN, Hageman MJ, Muraoka LM. Thermally induced denaturation of lyophilized bovine somatotropin and lysozyme as impacted by moisture and excipients. J Pharm Sci 1995; 84:707–712.
11. Franks F. Freeze Drying: a combination of physics, chemistry, engineering and economics. Jpn J Freezing Drying 1992; 38:5–16.
12. Pikal M. Freeze-drying of proteins. BioPharm 1990; 3:26–30.
13. Prestrelski SJ, Pikal KA, Arakawa T. Optimization of lyophilization conditions for recombinant human interleukin-2 by dried-state conformational analysis using Fourier-transform infrared spectroscopy. Pharm Res 1995; 12:1250–1259.
14. Duddu SP, Dal Monte PR. Effect of glass transition temperature on the stability of lyophilized formulations containing a chimeric therapeutic monoclonal antibody. Pharm Res 1997; 14:591–595.
15. Costantino HR, Langer R, Klivanov AM. Aggregation of a lyophilized pharmaceutical protein, recombinant human albumin: effect of moisture and stabilization by excipients. Bio/Technology 1995; 13:493–496.
16. Kalichevsky MT, Jaroszkiewicz EM, Ablett S, et al. The glass transition of amylopectin measured by DSC, DMTA and NMR. Carbohydr Polym 1992; 18:77–88.
17. Kalichevsky MT, Jaroszkiewicz EM, Blanshard JMV. A study of the glass transition of amylopectin-sugar mixtures. Polymer 1993; 34:346–358.
18. Oksanen CA, Zografi G. Molecular mobility in mixtrures of absorbed water and solid poly(vinylpyrrolidone). Pharm Res 1993; 10:791–799.
19. Yoshioka S, Aso Y, Otsuka T, et al. Water mobility in poly(ethylene glycol)-, poly(vinylpyrrolidone)-, and gelatin-water systems as indicated by dielectric relaxation time, spin-lattice relaxation time, and water activity. J Pharm Sci 1995; 84:1072–1077.
20. Rubin CA, Wasylyk JM, Baust JG. Investigation of vitrification by nuclear magnetic resonance and differential scanning calorimetry in honey: a model carbohydrate system. J Agric Food Chem 1990; 38:1824–1827.
21. Shamblin SL, Tang X, Chang L, et al. Characterization of the time scales of molecular motion in pharmaceutically important glasses. J Phys Chem 1999; 103:4113–4121.

22. Andronis V, Zografi G. The molecular mobility of supercooled amorphous indomethacin as a function of temperature and relative humidity. Pharm Res 1998; 15:835–842.
23. Liu J, Rigsbee DR, StotzandM C, et al. Dynamics of pharmaceutical amorphous solid: the study of enthalpy relaxation by isothermal microcalorimetry. J Pharm Sci 2002; 91:1853–1862.
24. Hancock BC, Shamblin SL, Zografi G. Molecular mobility of amorphous pharmaceutical solids below their glass transition temperatures. Pharm Res 1995; 12:799–806.
25. Andronis V, Zografi G. Molecular mobility of supercooled amorphous indomethacin, determined by dynamic mechanical analysis. Pharm Res 1997; 14:410–414.
26. Yoshioka S, Aso Y, Kojima S. Dependence of the molecular mobility and protein stability of freeze-dried γ-globulin formulations on the molecular weight of dextran. Pharm Res 1997; 14:736–741.
27. Yoshioka S, Aso Y, Nakai Y, et al. Effect of high molecular mobility of poly(vinyl alcohol) on protein stability of lyophilized γ-globulin formulations. J Pharm Sci 1998; 87:147–151.
28. Yoshioka S, Aso Y, Kojima S. The effect of excipients on the molecular mobility of lyophilized formulations, as measured by glass transition temperature and NMR relaxation-based critical mobility temperature. Pharm Res 1999; 16:135–140.
29. Yoshioka S, Aso Y, Kojima S. Different molecular motions in lyophilized protein formulations as determined by laboratory and rotating frame spin-lattice relaxation times. J Pharm Sci 2002; 91:2203–2210.
30. Chen Q, Yamada T, Kurosu H, et al. Dynamic study of the noncrystalline phase of ^{13}C-laveled polyethylene by variable-temperature ^{13}C CP/MAS NMR spectroscopy. J Polym Sci B 1992; 30:591–601.
31. Yoshioka S, Aso Y, Kojima S, et al. Molecular mobility of protein in lyophilized formulations linked to the molecular mobility of polymer excipients, as determined by high resolution ^{13}C solid-state NMR. Pharm Res 1999; 16:1621–1625.
32. Yoshioka S, Miyazaki T, Aso Y. β-Relaxation of insulin molecule in lyophilized formulations containing trehalose or dextran as a determinant of chemical reactivity. Pharm Res 2006; 23:961–966.
33. Yoshioka S, Miyazaki T, Aso Y, et al. Significance of local mobility in aggregation of β-galactosidase lyophilized with trehalose, sucrose or stachyose. Pharm Res 2006; 23:961–966.
34. Afonin S, Glaser RW, Berditchevskaia M, et al. 4-Fluorophenylglycine as a label for ^{19}F NMR structure analysis of membrane-associated peptides. Chembiochem 2003; 4:1151–1163.
35. Aso Y, Yoshioka S, Miyazaki T, et al. Feasibility of ^{19}F-NMR for assessing the molecular mobility of flufenamic acid in solid dispersions. Chem Pharm Bull (Tokyo) 2009; 57:61–64.
36. Hancock BC, Zografi G. Characteristics and significance of the amorphous state in pharmaceutical systems. J Pharm Sci 1997; 86:1–12.
37. Andronis V, Zografi G. Crystal nucleation and growth of indomethacin polymorphs from the amorphous state. J Non-Cryst Solids 2000; 271:236–248.
38. Aso Y, Yoshioka S, Kojima S. Explanation of the crystallization rate of amorphous nifedipine and phenobarbital from their molecular mobility as measured by ^{13}C NMR relaxation time and the relaxation time obtained from the heating rate dependence of T_g. J Pharm Sci 2001; 89:128–143.
39. Aso Y, Yoshioka S, Kojima S. Molecular mobility-based estimation of the crystallization rates of amorphous nifedipine and phenobarbital in poly(vinylpyrrolidone) solid dispersions. J Pharm Sci 2004; 93:384–391.
40. Korhonen O, Bhugra C, Pikal MJ. Correlation between molecular mobility and crystallization growth of amorphous phenobarbital and phenobaribita with polyvinylpyrrolidone and L-proline. J Pharm Sci 2008; 97:3830–3841.
41. Shamblin SL, Zografi G. Enthalpy relaxation in binary amorphous mixtures containing sucrose. Pharm Res 1998; 15:1828–1834.

42. Yoshioka S, Aso Y, Kojima S. Temperature dependence of bimolecular reactions associated with molecular mobility in lyophilized formulations. Pharm Res 2000; 17:923–927.
43. Yoshioka S, Tajima S, Aso Y, et al. Inactivation and aggregation of β-galactosidase in lyophilized formulation described by the Kohlrausch-Williams-Watts stretched exponential function. Pharm Res 2003; 20:1655–1660.
44. Yoshioka S, Aso Y, Miyazaki T. Negligible contribution of molecular mobility to degradation rate of insulin lyophilized with poly(vinylpyrrolidone). J Pharm Sci 2006; 95:939–943.

International Journal of Pharmaceutics 407 (2011) 111–118

Contents lists available at ScienceDirect

International Journal of Pharmaceutics

journal homepage: www.elsevier.com/locate/ijpharm

Differences in crystallization rate of nitrendipine enantiomers in amorphous solid dispersions with HPMC and HPMCP

Tamaki Miyazaki[a,*], Yukio Aso[a], Sumie Yoshioka[b], Toru Kawanishi[a]

[a] Division of Drugs, National Institute of Health Sciences, 1-18-1 Kamiyoga, Setagaya-ku, Tokyo 158-8501, Japan
[b] School of Pharmacy, University of Connecticut, Storrs, CT, United States

ARTICLE INFO

Article history:
Received 21 October 2010
Received in revised form
21 December 2010
Accepted 19 January 2011
Available online 26 January 2011

Keywords:
Nitrendipine
Enantiomer
Chiral polymer
Solid dispersions
Crystallization

ABSTRACT

To clarify the contribution of drug–polymer interaction to the physical stability of amorphous solid dispersions, we studied the crystallization rates of nitrendipine (NTR) enantiomers with identical physicochemical properties in the presence of hydroxypropylmethylcellulose (HPMC), hydroxypropylmethylcellulose phthalate (HPMCP) and polyvinylpyrrolidone (PVP). The overall crystallization rate at 60 °C and the nucleation rate at 50–70 °C of (+)-NTR were lower than those of (−)-NTR in the presence of 10–20% HPMC or HPMCP. In contrast, similar crystallization profiles were observed for the NTR enantiomers in solid dispersions containing PVP. The similar glass transition temperatures for solid dispersions of (−)-NTR and (+)-NTR suggested that the molecular mobility of the amorphous matrix did not differ between the enantiomers. These results indicate that the interaction between the NTR enantiomers and HPMC or HPMCP is stereoselective, and that differences in the stereoselective interaction create differences in physical stability between (−)-NTR and (+)-NTR at 50–70 °C. However, no difference in physical stability between the enantiomers was obvious at 40 °C. Loss of the difference in physical stability between the NTR enantiomers suggests that the stereoselective interaction between NTR and the polymers may not contribute significantly to the physical stabilization of amorphous NTR at 40 °C.

1. Introduction

Nifedipine analogues are used for treatment of cardiovascular disorders. Most of them are poorly water soluble and their bioavailability is low when administered orally in crystal form. To improve the bioavailability by increasing the dissolution rate and solubility, amorphous solid dispersions of nifedipine analogues have been studied over the past few decades (Suzuki and Sunada, 1998; Chutimaworapan et al., 2000; Vippagunta et al., 2002; Hirasawa et al., 2003a,b, 2004; Tanno et al., 2004; Karavas et al., 2005, 2006; Wang et al., 2005, 2007; Kim et al., 2006; Konno and Taylor, 2006; Huang et al., 2008; Marsac et al., 2008; Rumondor et al., 2009a,b). Drugs in an amorphous state are more easily dissolved in water than their crystalline counterparts. However, recrystallization to a thermodynamically stable form during long-term storage is a matter of concern. The physical stability of amorphous solid dispersions (crystallization tendency) has been reported to correlate with several factors, such as molecular mobility (Aso et al., 2004; Miyazaki et al., 2007), drug–excipient interactions and miscibility (Matsumoto and Zografi, 1999; Marsac et al., 2006, 2009; Miyazaki et al., 2004, 2006, 2007; Konno and Taylor, 2006; Haddadin et al., 2009; Tao et al., 2009; Telang et al., 2009). The crystallization rate of amorphous nitrendipine (NTR) increases with a decrease in the glass transition temperature (T_g) associated with water sorption, indicating that molecular mobility, in terms of T_g, is correlated with physical stability. However, amorphous nilvadipine is more stable than nifedipine, even though the two had similar T_g values, indicating that the difference in physical stability between nilvadipine and nifedipine might be attributable to differences in chemical structure (Miyazaki et al., 2007). Hydrogen bond interaction between felodipine and hydroxypropylmethylcellulose (HPMC) or hydroxypropylmethylcellulose acetate succinate is considered to decrease the nucleation rate of felodipine, since no significant change in molecular mobility, reflected in T_g value, has been observed (Konno and Taylor, 2006). Also, drug–excipient miscibility is reportedly related to the physical stability of nifedipines. Drug crystallization has been observed to occur earlier in solid dispersions showing phase separation due to low miscibility of the drug with the excipient polymers (Rumondor et al., 2009a,b; Marsac et al., 2010). In order to develop stable amorphous solid dispersions, it is important to clarify the relative significance of these factors for the physical stability of amorphous solid dispersions. Therefore, designing a model system that is as simple as possible is the key to evaluation of each individual factor.

NTR has an asymmetric carbon (Fig. 1), and is available as a mixture of both enantiomers. These enantiomers can be resolved by chiral chromatography. Since both enantiomers have identical physical and chemical properties, including molecular mass, T_g,

* Corresponding author. Tel.: +81 3 3700 1141; fax: +81 3 3707 6950.
E-mail address: miyazaki@nihs.go.jp (T. Miyazaki).

0378-5173/$ – see front matter © 2011 Elsevier B.V. All rights reserved.
doi:10.1016/j.ijpharm.2011.01.035

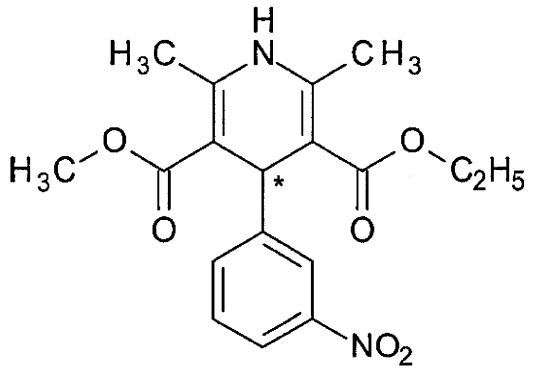

Fig. 1. Chemical structure of NTR. The asterisk represents asymmetric carbon.

melting point and density, the effects of molecular mobility and chemical structure on their physical stability are expected to be the same. Therefore, solid dispersions of NTR enantiomers may provide a useful model system for studies of drug–polymer stereoselective interaction. In the present study, HPMC and hydroxypropylmethylcellulose phthalate (HPMCP) were used as chiral polymers, and polyvinylpyrrolidone (PVP), an achiral polymer, was selected as a control to investigate the effect of drug–polymer interaction on the physical stability of amorphous NTR enantiomers. The overall crystallization rates were determined from the time-profiles of amorphous drug remaining, as measured by differential scanning calorimetry (DSC). Furthermore, the nucleation and the crystal growth rates of each NTR enantiomer in the solid dispersions containing HPMC, HPMCP or PVP were determined by polarized light microscopy. Measurements of T_g and Fourier-transform infrared spectra (FT-IR) were carried out for evaluation of molecular mobility and drug–polymer interactions, respectively.

2. Materials and methods

2.1. Materials

PVP (PVP10) and HPMC (USP grade) were purchased from Sigma–Aldrich, Inc. HPMCP (HP-55) was kindly obtained from Shin-Etsu Chemical Co., Ltd.

NTR (Wako Pure Chemical Industries Ltd.) was resolved on a CHIRALCEL OJ-H column (Daicel Chemical Industries, Ltd., 10 mm × 250 mm) into two fractions of each enantiomer with a mobile phase of n-hexane/ethanol (100/15, flow rate: 4 ml/min). A 500 μl of 1% NTR solution in n-hexane/ethanol (1/1) was injected, and ultraviolet spectrophotometric detection was carried out at 254 nm. The circular dichroism spectrum of the first fraction exhibited a negative peak at around 360 nm, and the second one exhibited a positive peak. Therefore, the first and second fractions of NTR were designated (−)-NTR and (+)-NTR, respectively. The optical purity of each enantiomer was determined to be more than 99.96%, and the amount of photo degradation product of NTR was determined to be less than 0.03% by liquid chromatography, on a CHIRALCEL OJ-H column (Daicel Chemical Industries, Ltd.,

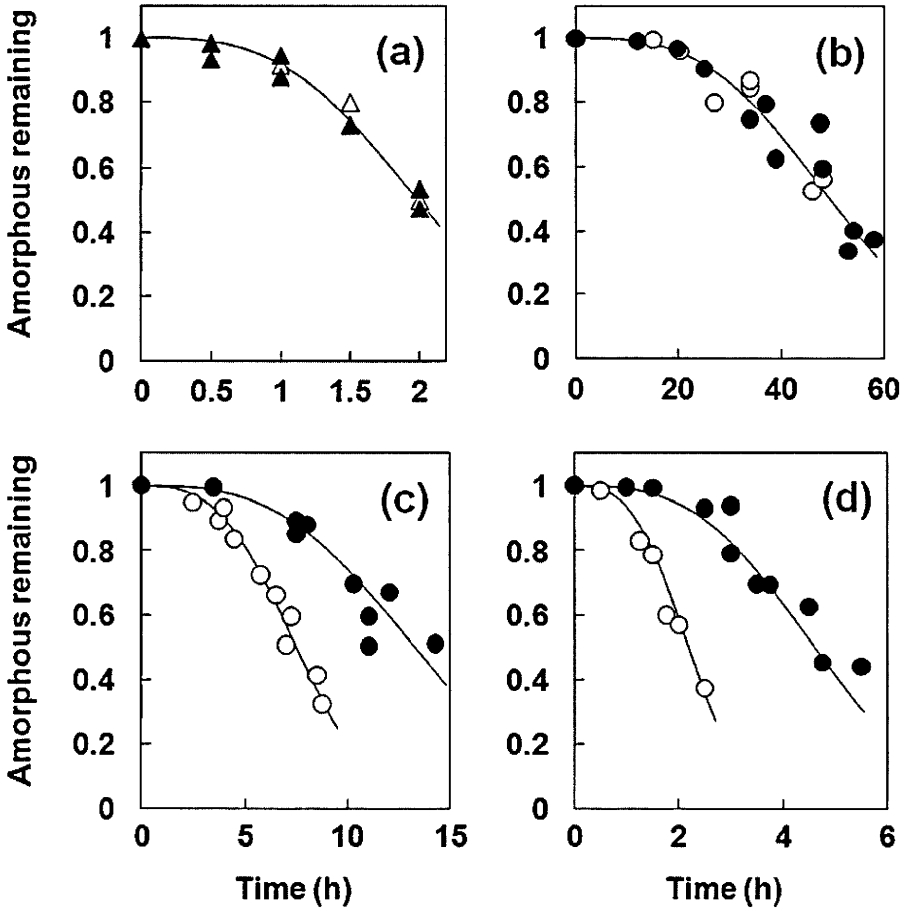

Fig. 2. Crystallization profiles of each NTR enantiomer alone ((a); △, ▲) and the enantiomers in solid dispersions (○, ●) with (b) 10% PVP, (c) 10% HPMC and (d) 10% HPMCP at 60 °C. Open symbols represent (−)-NTR and solid symbols represent (+)-NTR. The lines in the figures represent the best fit of the Avrami equation.

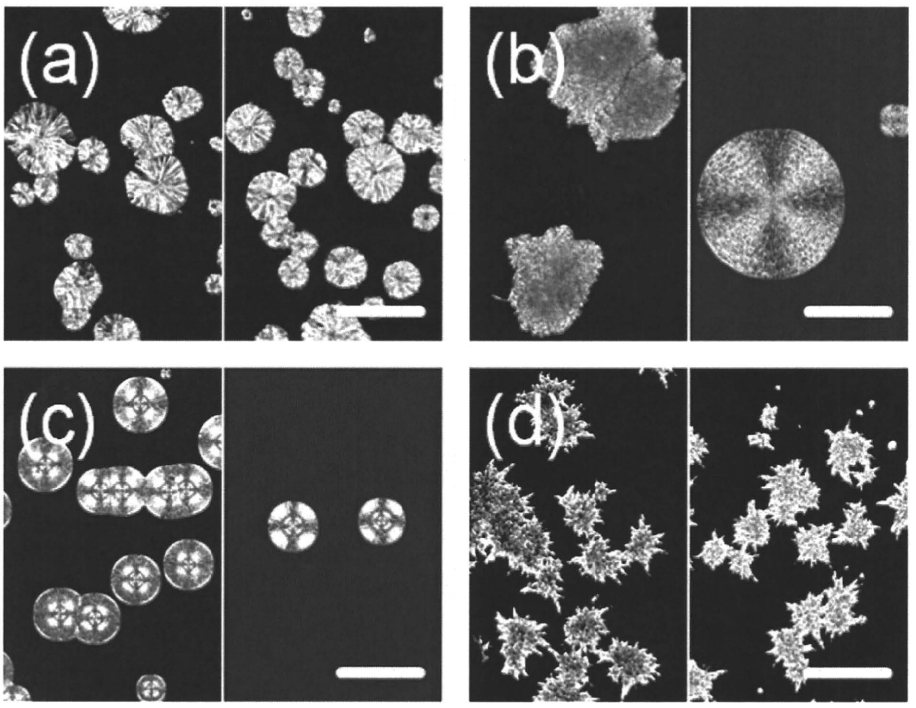

Fig. 3. Typical crystal shape observed for the amorphous NTR enantiomers and their solid dispersions: (a) without polymer, (b) 10% HPMC, (c) 10% HPMCP and (d) 10% PVP. The left side of each micrograph was taken from the (−)-NTR samples, and the right side from the (+)-NTR samples. The bars in the micrographs correspond to 100 μm.

4.6 mm × 250 mm) with a mobile phase of n-hexane/ethanol = 10/1 (1 ml/min). Since NTR is a photo sensitive compound, NTR samples were handled under dim light (<120 lx).

2.2. Determination of the overall crystallization rate of amorphous NTR enantiomers

Amorphous solid dispersions of the NTR enantiomers were prepared by melt-quenching drug–polymer mixtures. One NTR enantiomer and a polymer were initially dissolved in a solvent that was suitable for both components. Ethanol/acetone (1:1) was used for the NTR–HPMC and NTR–HPMCP combinations, and ethanol was used for the NTR–PVP combination. Next, the solvent was rotary-evaporated to obtain a homogeneous drug–polymer mixture. Approximately 4 mg of the pulverized mixture was weighed into an aluminum pan for DSC, and was kept at around 180 °C in the cell of a DSC (DSC2920, TA Instruments) for approximately 2 min under dry nitrogen gas flow (30 ml/min). The melted sample was transferred to a desiccator containing phosphorus pentoxide, and the desiccator was stored at a constant temperature of 30–70 °C. For the pure NTR enantiomer, the resolved enantiomer crystal (4 mg) was melt-quenched as described above to obtain an amorphous sample.

After certain periods of time, the change in heat capacity (ΔC_p) at T_g was measured for the stored amorphous samples by DSC at a heating rate of 20 °C/min. The amount of amorphous drug remaining in the sample at time t, $x(t)$, was calculated according to Eq. (1):

$$x(t) = \frac{\Delta C_{pt}}{\Delta C_{p0}} \tag{1}$$

where ΔC_{pt} and ΔC_{p0} are the ΔC_p values at time t and initially, respectively. The time required for 10% of the amorphous NTR to crystallize (t_{90}) was estimated as an indicator of the crystallization tendency. The time-profiles of $x(t)$ were analyzed according to the Avrami equation (Eq. (2), $n = 3$) to calculate t_{90}:

$$x(t) = \exp[-kt^n] \tag{2}$$

where k is the crystallization rate constant and n is the Avrami index. HPLC analysis of stored NTR samples showed no evidence of degradation during melt-quenching and subsequent storage.

2.3. Determination of nucleation rate and crystal growth rate of NTR enantiomer

The nucleation rate and the crystal growth rate were determined for samples prepared in a space between two glass disks separated by a stainless steel ring. The NTR enantiomer–polymer mixture, which was described above, or the crystalline NTR enantiomer (1.5–2 mg) was placed on a clean glass disk (thickness: 0.12 mm, diameter: 16 mm) and heated at 180 °C in the DSC with a stainless steel ring (inner diameter: 6 mm, thickness: 20 μm) as a spacer. After the sample had melted completely, it was covered with another glass disk (thickness: 0.12 mm, diameter: 12 mm) to yield an amorphous layer between the glasses. Attention was paid to ensure that the layer was free of bubbles. For measurements at temperatures above 40 °C, the sample was stored in the chamber of a heating/cooling stage for microscopy (THMS600, Linkam Scientific Instruments), which had been adjusted to a prescribed temperature in advance. The moisture in the chamber was removed by purging with dry nitrogen gas for 10–15 min. Microscopic images of the sample were recorded at appropriate time intervals by a digital camera (DXM1200F, Nikon Corporation) attached to a polarized light microscope (ECLIPSE E600 POL, Nikon Corporation) with a 10× objective lens. In order to minimize possible photo degradation of NTR by the polarized light, the light source of the microscope was shut off when images were not recorded. For measurements at 30 °C, the samples were stored at 30 °C in desiccators containing phosphorous pentoxide. After an appropriate period of storage, microscopic images of the sample were recorded, and the sample was again stored at 30 °C in a dry state.

2.3.1. Measurement of nucleation rate

The nucleation rate of the NTR enantiomers was estimated from time-profiles of nucleation site density determined from microscopic images of the stored samples. Nucleation site density per unit volume was calculated from the number of nucleation sites per unit area and the depth of field of the lens used for data collection. The depth of field was calculated to be 8.46 μm from the wavelength of the light (546 nm) and the numerical aperture of the lens (0.25). For samples with more than a dozen nucleation sites per fixed field at the end of the observation period, nucleation sites were counted in one fixed field. For samples with less than a dozen nucleation sites per field near the end of the observation period, and those stored at 30 °C, nucleation sites were counted for 12 individual areas in one sample, and the average value from the 12 individual images was regarded as the number of nucleation sites per field. The nucleation rate was obtained from the slope of time-profiles of the number of nucleation sites per unit volume (nucleation site density) at steady state. In cases showing preferential nucleation and growth at the sample periphery, these sites were not included in the analysis. The reported nucleation rates were average values of those obtained for at least three samples prepared separately.

2.3.2. Measurement of crystal growth rate

The crystal growth rates at temperatures above 40 °C were measured concurrently with the nucleation rate measurements as described above. The measurements at 30 °C were carried out using samples that showed more than a dozen nucleation sites per one field after a few months of storage in desiccators containing phosphorous pentoxide. The sample was placed in the chamber of the heating/cooling stage controlled at 30 °C, and the growth of crystals was observed in a fixed field. The radius of each crystal was estimated from a circular approximation by using Lumina Vision software (Mitani Co.). The average crystal growth rate was calculated from the increase in the radius as a function of time based on observations of at least 20 crystals.

2.4. FT-IR

FI-IR spectra were collected using a FT/IR-6300 (JASCO Corporation) by the KBr method at ambient room temperature. Transmission spectra were obtained for KBr disks containing 1–1.5% sample at a resolution of 0.4 cm^{-1} within the range of 4000–400 cm^{-1}. An accumulation of 128–256 scans was acquired for each disk.

3. Results

3.1. Effects of polymers on the overall crystallization rates of NTR enantiomers in solid dispersions

No significant differences in the melting point (158 °C), T_g (33 °C) and ΔC_p at T_g (0.40 J/g/K) were observed between (−)-NTR and (+)-NTR. Table 1 shows the T_g values of amorphous solid dispersions of (−)-NTR and (+)-NTR. There appeared to be no significant difference in the T_g values between the two. The solid dispersions containing HPMC (10–20%) and 5% PVP showed T_g values similar to that of each NTR enantiomer alone. T_g values for solid dispersions containing 10% PVP were slightly higher than that of each NTR enantiomer alone, whereas solid dispersions containing HPMCP (10–20%) exhibited T_g values slightly lower than that of each NTR enantiomer alone.

Fig. 2 shows time-profiles of overall crystallization of NTR enantiomers at 60 °C. No significant differences in the overall crystallization profiles were observed between (−)-NTR and (+)-NTR without polymer (Fig. 2(a)), and between (−)-NTR and (+)-NTR in solid dispersions containing 10% PVP (Fig. 2(b)). In contrast, differences in time-profiles between the enantiomers were observed for solid dispersions containing 10% HPMC or HPMCP: (+)-NTR crystallized more slowly than (−)-NTR, as shown in Fig. 2(c) and (d). Table 2 shows the t_{90} values for the amorphous NTR enantiomers obtained for NTR alone and NTR in the solid dispersions. The t_{90} values for (−)-NTR without polymer and those of solid dispersions containing 5–10% PVP were almost the same as the t_{90} values for (+)-NTR without polymer and those of solid dispersions containing 5–10% PVP, respectively, at the temperatures studied. The t_{90} values at 50 and 60 °C for (+)-NTR were 1.5–2.0 times longer than that for (−)-NTR in solid dispersions containing 10–20% HPMC or HPMCP. At 40 °C, however, any difference between the enantiomers was not clear.

Table 1
T_g of pure NTR enantiomers and their solid dispersions with a polymer.

Polymer	Polymer content [%]	T_g[a] [°C]	
		(−)-NTR	(+)-NTR
None	0	33.2 ± 0.1	33.1 ± 0.2
HPMC	10	33.1 ± 1.0	33.0 ± 0.7
	20	33.1 ± 0.8	33.0 ± 0.7
HPMCP	10	31.2 ± 0.7	31.0 ± 0.4
	20	30.8 ± 1.2	30.5 ± 0.9
PVP	5	33.0 ± 0.2	33.1 ± 0.2
	10	36.3 ± 1.2	36.2 ± 0.8

[a] Average ± standard deviation (n = 3).

3.2. Effects of polymers on the nucleation rate and crystal growth rate

Fig. 3 shows the typical micrographs of NTR crystals grown from amorphous pure enantiomers and their solid dispersions with a polymer. The recrystallized NTR enantiomers without polymers showed a melting point of 158 °C, suggesting the same crystal form as the originally resolved stable one. The melting point of the samples containing 10% HPMC, HPMCP and PVP was approximately 151 °C in all cases, regardless of the various crystal shapes shown in Fig. 3. The difference from the melting point of the pure enantiomers would have been due to melting point depression by the

Table 2
t_{90} for NTR enantiomers with and without polymer.

Temperature [°C]	Polymer	[%]	t_{90}[a] [h]			
			(−)-NTR		(+)-NTR	
40	None	0	41	(1)	41	(1)
	HPMC	10	230, 240[b]		230, 230[b]	
	HPMCP	10	49	(1)	49	(1)
50	None	0	5.7	(0.2)	5.7	(0.1)
	PVP	10	250	(10)	240	(4)
	HPMC	10	17	(0.4)	25	(0.1)
	HPMCP	10	6.1	(0.3)	11	(0.3)
60	None	0	1.1	(0.1)	1.1	(0.1)
	PVP	5	3.5	(0.1)	3.6	(0.1)
		10	25 ± 3[c]		25 ± 3[c]	
	HPMC	10	3.8, 4.1[b]		6.7, 6.9[b]	
		20	8.7	(0.3)	15	(0.4)
	HPMCP	10	1.5 ± 0.2[c]		2.7 ± 0.3[c]	
		20	3.2	(0.1)	6.4	(0.2)

[a] The values in parentheses are standard error estimated from single experiments using Origin 8.1 software (Lightstone Corp.).

[b] Results with two values represent the results obtained from duplicate experiments using separately prepared samples.

[c] Mean ± standard deviation (n = 3).

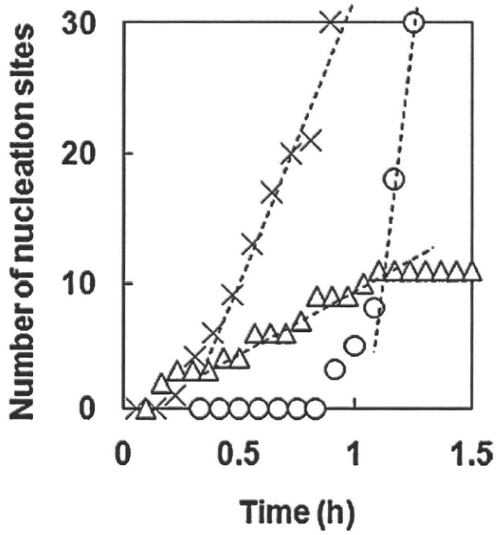

Fig. 4. Time profiles of the number of nucleation sites per field of view for (+)-NTR at 50 °C (○), 60 °C (×) and 70 °C (△). The dotted lines show the linear regression at steady state.

added polymers, as the melting point fell gradually with increasing polymer content (data not shown). The data suggested that differences in crystal habit, rather than polymorphism, might have been responsible for the differences in crystal shape among the solid dispersions.

Fig. 4 shows the typical time-profiles of the nucleation of amorphous NTR enantiomer stored at various temperatures. The lower the storage temperature, the longer the period required before the first crystal was observed. The nucleation rates at steady state were obtained from the slope of the lines in Fig. 4, and these were plotted against storage temperature (Fig. 5). As expected from the similar overall crystallization profiles of the NTR enantiomers (Fig. 2(a) and (b)), no significant difference in the nucleation rates between (−)-NTR and (+)-NTR was observed for amorphous NTR alone and the solid dispersions containing PVP within the temperature range studied (Fig. 5(a)). In contrast, the nucleation rates of (+)-NTR were lower than those of (−)-NTR in the solid dispersions containing HPMC and HPMCP (Fig. 5(b)) within the temperature range of 50–70 °C. At 40 °C, however, the differences in the rates between (−)-NTR and (+)-NTR were not pronounced. These results were consistent with the t_{90} values of the enantiomers shown in Table 2.

Fig. 6 shows the typical time-profiles of the NTR crystal growth at 60 °C. Crystal radius increased linearly with time, and the growth rate was estimated from linear regression of the plots. The higher the temperature, the faster the crystals grew within the temperature range studied (Fig. 7). In contrast to the nucleation rates, no significant growth rate differences between the NTR enantiomers were observed, irrespective of the absence or presence of any polymer.

3.3. FT-IR

FT-IR spectra (4000–400 cm^{-1}) of (−)-NTR and (+)-NTR were indistinguishable from one another for both the amorphous and the crystalline forms. Similarly, the FT-IR spectra of amorphous solid dispersions were almost the same for (−)-NTR and (+)-NTR with any polymer. Fig. 8 shows the spectra for crystalline (−)-NTR (dotted line in Fig. 8 (a)), NTR solid dispersions containing 25–75% HPMC and HPMC alone (dotted line in Fig. 8 (c)) in the range of 1800–1550 cm^{-1}, corresponding to C=O stretching region of NTR. Spectra with and without an asterisk represent that of (−)-NTR

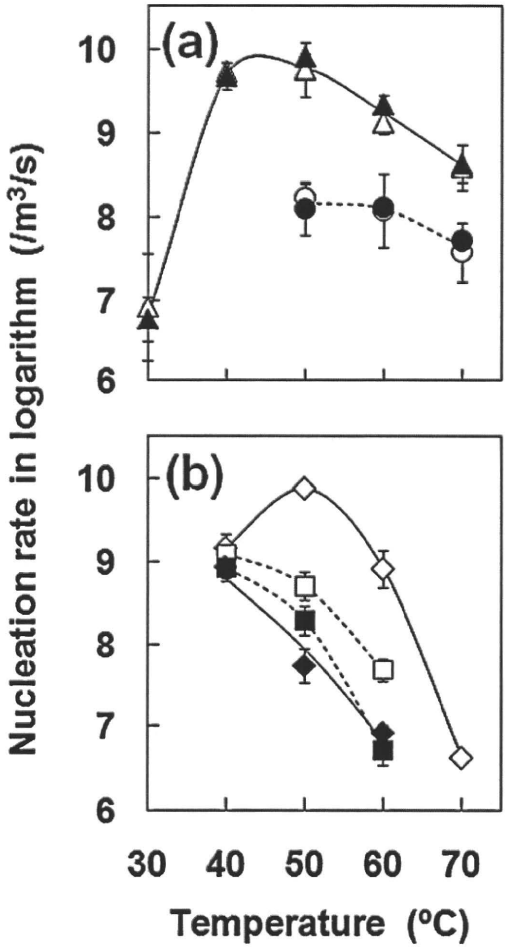

Fig. 5. Plots of nucleation rate as a function of temperature. Error bars represent standard deviation for at least triplicate experiments. (a) △, ▲: without polymer, ○, ●: 10% PVP and (b) □, ■: 10% HPMC, ◇, ♦: 10% HPMCP. Open symbols represent (−)-NTR and solid symbols represent (+)-NTR.

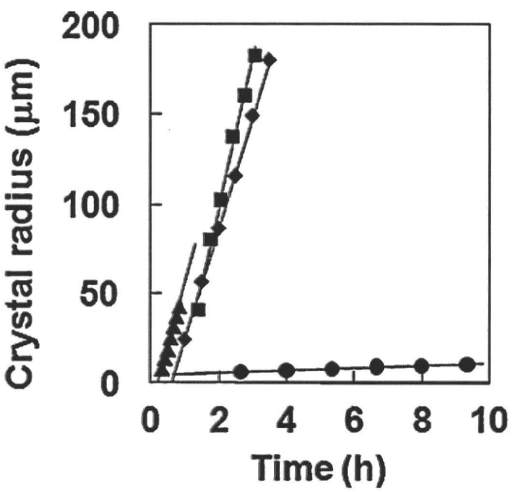

Fig. 6. Typical time profiles of the radius of NTR crystals in (+)-NTR alone (▲), and solid dispersions with 10% HPMC (■), 10% HPMCP (♦) and 10% PVP (●) at 60 °C.

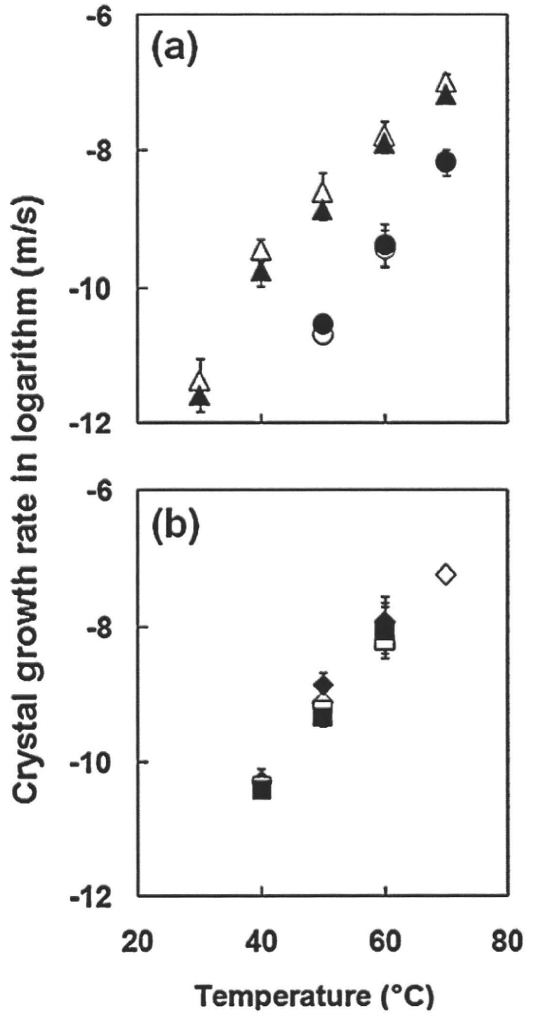

Fig. 7. Temperature dependence of crystal growth rate of NTR enantiomers. Error bars represent standard deviation for at least triplicate experiments. (a) △, ▲: without polymer; ○, ●: 10% PVP and (b) □, ■: 10% HPMC; ◇, ◆: 10% HPMCP. Open symbols represent (−)-NTR and solid symbols represent (+)-NTR.

and (+)-NTR, respectively. Despite its vicinity to the asymmetric carbon, carbonyl group of (−)-NTR and (+)-NTR showed same spectra even in the presence of HPMC. Likewise, no difference in spectra between solid dispersions of (−)-NTR and (+)-NTR containing HPMCP was observed (data not shown).

Fig. 9 shows the spectra in the range of 3650–3150 cm^{-1}, corresponding to NH stretching vibrations of nifedipine derivatives (Konno and Taylor, 2006), where the changes in peak position were obvious upon mixing with polymers as solid dispersions. There were also no obvious differences in the spectra between the two enantiomers. The peak around 3350 cm^{-1} was assigned to the NH stretching vibration that was expected to be involved in the hydrogen bonding between the drug and a polymer. The peak position was shifted from 3360 cm^{-1} to 3337 cm^{-1} by amorphization, and additionally shifted to 3291 cm^{-1} in the presence of 50% PVP (Figs. 9(b) and 10). On the other hand, for solid dispersions prepared with HPMC and HPMCP, the peak position showed a degree of shift to a higher wavenumber (Figs. 9(c) and (d) and 10). The peak position for solid dispersions with 75% HPMCP was nearly equal to that of the pure NTR crystals. These changes in peak position showed the same tendency for both (+)-NTR and (−)-NTR.

4. Discussion

The overall crystallization of (−)-NTR proceeded faster than that of (+)-NTR in solid dispersions with HPMC or HPMCP (Fig. 2(c) and (d)), while that for solid dispersions with PVP proceeded at almost the same rate, regardless of NTR chirality (Fig. 2(b)). The nucleation rates of (−)-NTR were greater than those of (+)-NTR in solid dispersions with HPMC or HPMCP at 50–70 °C (Fig. 5(b)), while no difference in nucleation rates between the NTR enantiomers was observed for solid dispersions with PVP (Fig. 5(a)). The T_g values for samples using (−)-NTR or (+)-NTR were almost the same (Table 1), suggesting that the differences in the overall crystallization profiles and nucleation rates between the enantiomers are not due to differences in molecular mobility between (−)-NTR and (+)-NTR in solid dispersions with HPMC or HPMCP. The difference in physical stability between the two enantiomers may be explained by the difference in strength of NTR–polymer interaction between them. The results obtained from FT-IR measurements indicate that PVP interacts with NTR through hydrogen bonding at the NH moiety of NTR (Figs. 9 and 10). Almost the same degrees of shift in wavenumber for NH stretching suggest a similar strength of hydrogen bond interaction for (−)-NTR and (+)-NTR. PVP polymer chains possess an asymmetric carbon in a monomer unit, and are composed of monomer units with an equal ratio of R and S configurations. Therefore, (−)-NTR and (+)-NTR are considered to interact with PVP through hydrogen bonds of the same strength and number, resulting in a similar degree of physical stability between (−)-NTR and (+)-NTR. In contrast, HPMC and HPMCP are cellulose derivatives that are polymers of optically active D-glucose, and thus are expected to interact differently (strength and/or number) with NTR enantiomers, resulting in the difference in physical stability between (−)-NTR and (+)-NTR, although differences in interaction were not detectable by FT-IR. At 40 °C, however, the differences in physical stability between the enantiomers with HPMC or HPMCP were not remarkable (Table 2, Fig. 5). We do not have a satisfactory explanation for the loss of the difference in stabilization by HPMC and HPMCP. However, one possible explanation is as follows: The temperature dependence of the nucleation rate exhibits a maximum just above T_g because the nucleation rate is influenced by both molecular mobility and thermodynamic factors; an increase of temperature increases the molecular mobility, and thus the nucleation rate, whereas nucleation is thermodynamically favored at lower temperatures. A barrier due to molecular mobility is considered to play a predominant role in nucleation within the temperature range below the maximum point (Hancock and Zografi, 1997; Andronis and Zografi, 2000). Therefore, loss of the difference in physical stability between the enantiomers at 40 °C may be due to the predominant contribution of molecular mobility, since the molecular mobility is suggested to be similar for (−)-NTR and (+)-NTR in solid dispersions, as indicated by the T_g values (Table 1). However, physical stability data at temperatures below 40 °C, which are difficult to obtain within the commonly used experimental time scale, are needed in order to support this speculation.

In contrast to the nucleation rates, no significant difference in the crystal growth rates between the NTR enantiomers was observed for solid dispersions with HPMC or HPMCP (Fig. 7). The crystal growth rates for solid dispersions with HPMC or HPMCP were similar to those for each NTR enantiomer alone, indicating that the effects of HPMC and HPMCP on the crystal growth rate were small. This might be one of the reasons why differences in the crystal growth rate between the NTR enantiomers could not be detected in solid dispersions with HPMC or HPMCP.

It may be worth to note that PVP decreased the crystal growth rate of NTR enantiomers more than HPMC and HPMCP at all the temperatures studied (Fig. 7). On the other hand, PVP did not always decrease the nucleation rate of NTR more effectively than HPMC or

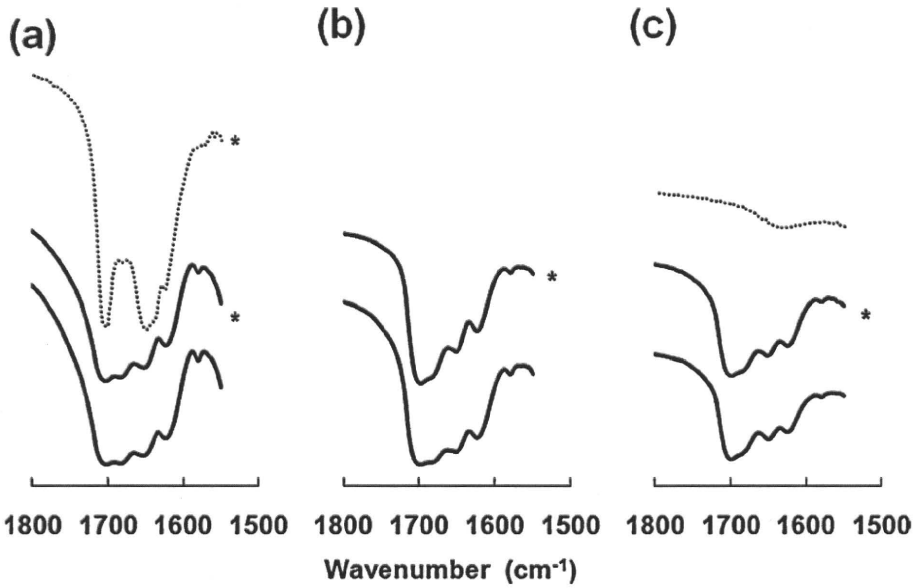

Fig. 8. FT-IR spectra of crystalline (−)-NTR, solid dispersions of NTR enantiomer containing HPMC, and HPMC alone. HPMC content was (a) 25% (b) 50%, and (c)75%. Dotted line in (a) represents the spectrum for crystalline (−)-NTR, and dotted line in (c) represents the spectrum for HPMC alone. The spectra with an asterisk are those of (−)-NTR.

HPMCP. For example, the nucleation rate of NTR at 60 °C was following order; (−)-NTR, (+)-NTR ≈ (−)-NTR–HPMCP > (−)-NTR–PVP, (+)-NTR–PVP > (−)-NTR–HPMC > (+)-NTR–HPMC, (+)-NTR–HPMCP (Fig. 5). PVP seems to decrease the crystal growth rate more effectively than the nucleation rate of NTR, whereas HPMC and HPMCP decrease only the nucleation rate of NTR. The reason for the different stabilizing effects of the polymers for the nucleation and crystal growth of NTR is not clear. The growth rate of NTR may only be decreased by strong interactions such as hydrogen bonding between NTR and PVP, which is detectable by FT-IR (Figs. 9 and 10). Weak drug–polymer interactions, which are not detectable by FT-IR, may decrease the nucleation rate of NTR, as well as hydrogen bond interactions between drug and polymer.

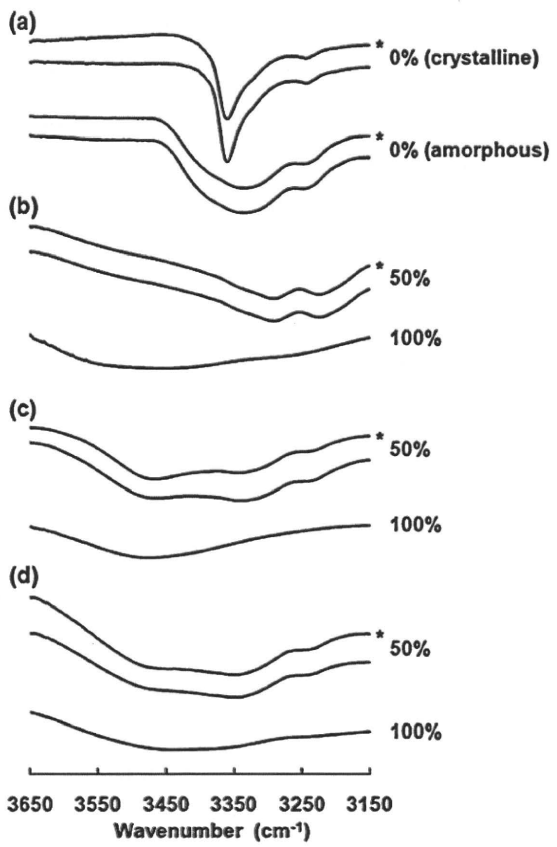

Fig. 9. FT-IR spectra of (a) crystalline and amorphous NTR enantiomers, and their amorphous solid dispersions with (b) PVP, (c) HPMC and (d) HPMCP. Percentages represent the weight percentage of polymer in the solid dispersions. The spectra with an asterisk are those of (−)-NTR.

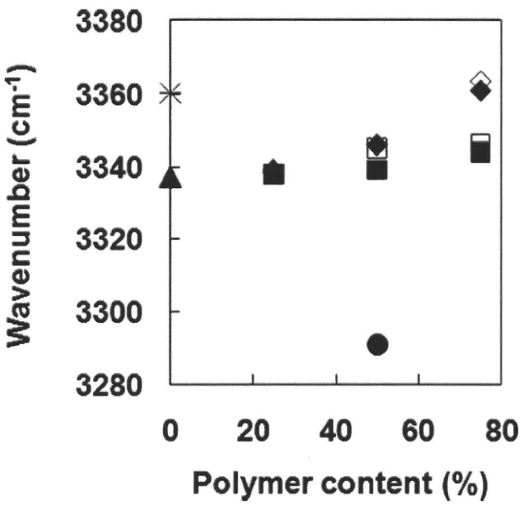

Fig. 10. Changes in FT-IR peak position showing the NH stretching region. +: (−)-NTR without polymer (crystalline); ×: (+)-NTR without polymer (crystalline); △, ▲: without polymer (amorphous); □, ■: HPMC; ◊, ♦: HPMCP; ○, ●: PVP. Open symbols represent (−)-NTR and solid symbols represent (+)-NTR.

5. Conclusions

Using NTR enantiomers as model drugs, the effects of stereoselective drug–polymer interaction on the crystallization rate of amorphous solid dispersions were elucidated. The chiral polymers, HPMC and HPMCP, retarded the crystallization of (+)-NTR more

effectively than that of (−)-NTR. The difference in physical stability at 50–70 °C would be due to stereoselective interaction. Stereoselective interaction affected the nucleation process more markedly than the crystal growth process. Since the stereoselective interaction between NTR enantiomers and HPMC or HPMCP would have been relatively weak, the impact of the interaction on the physical stability of amorphous NTR solid dispersions was obscure at room temperature.

Acknowledgements

Part of this work was supported by a Grant-in-aid for Research on Publicly Essential Drugs and Medical Devices from the Japan Health Sciences foundation.

References

Andronis, V., Zografi, G., 2000. Crystal nucleation and growth of indomethacin polymorphs from the amorphous state. J. Non-Cryst. Solids 271, 236–248.

Aso, Y., Yoshioka, S., Kojima, S., 2004. Molecular mobility-based estimation of the crystallization rates of amorphous nifedipine and phenobarbital in poly(vinylpyrrolidone) solid dispersions. J. Pharm. Sci. 93, 384–391.

Chutimaworapan, S., Ritthidej, G.C., Yonemochi, E., Oguchi, T., Yamamoto, K., 2000. Effect of water-soluble carriers on dissolution characteristics of nifedipine solid dispersions. Drug Dev. Ind. Pharm. 26, 1141–1150.

Haddadin, R., Qian, F., Desikan, S., Hussain, M., Smith, R.L., 2009. Estimation of drug solubility in polymers via differential scanning calorimetry and utilization of the fox equation. Pharm. Dev. Technol. 14, 18–26.

Hancock, B.C., Zografi, G., 1997. Characteristics and significance of the amorphous state in pharmaceutical systems. J. Pharm. Sci. 86, 1–12.

Hirasawa, N., Ishise, S., Miyata, H., Danjo, K., 2003a. Physicochemical characterization and drug release studies of nilvadipine solid dispersions using water-insoluble polymer as a carrier. Drug Dev. Ind. Pharm. 29, 339–344.

Hirasawa, N., Ishise, S., Miyata, H., Danjo, K., 2003b. An attempt to stabilize nilvadipine solid dispersion by the use of ternary systems. Drug Dev. Ind. Pharm. 29, 997–1004.

Hirasawa, N., Ishise, S., Miyata, H., Danjo, K., 2004. Application of nilvadipine solid dispersion to tablet formulation and manufacturing using crospovidone and methylcellulose as dispersion carriers. Chem. Pharm. Bull. 52, 244–247.

Huang, J., Wigent, R.J., Schwartz, J.B., 2008. Drug–polymer interaction and its significance on the physical stability of nifedipine amorphous dispersion in microparticles of an ammonio methacrylate copolymer and ethylcellulose binary blend. J. Pharm. Sci. 97, 251–262.

Karavas, E., Ktistis, G., Xenakis, A., Georgarakis, E., 2005. Miscibility behavior and formation mechanism of stabilized felodipine-polyvinylpyrrolidone amorphous solid dispersions. Drug Dev. Ind. Pharm. 31, 473–489.

Karavas, E., Ktistis, G., Xenakis, A., Georgarakis, E., 2006. Effect of hydrogen bonding interactions on the release mechanism of felodipine from nanodispersions with polyvinylpyrrolidone. Eur. J. Pharm. Biopharm. 63, 103–114.

Kim, E.J., Chun, M.K., Jang, J.S., Lee, I.H., Lee, K.R., Choi, H.K., 2006. Preparation of a solid dispersion of felodipine using a solvent wetting method. Eur. J. Pharm. Biopharm. 64, 200–205.

Konno, H., Taylor, L.S., 2006. Influence of different polymers on the crystallization tendency of molecularly dispersed amorphous felodipine. J. Pharm. Sci. 95, 2692–2705.

Marsac, P.J., Shamblin, S.L., Taylor, L.S., 2006. Theoretical and practical approaches for prediction of drug–polymer miscibility and solubility. Pharm. Res. 23, 2417–2426.

Marsac, P.J., Konno, H., Rumondor, A.C., Taylor, L.S., 2008. Recrystallization of nifedipine and felodipine from amorphous molecular level solid dispersions containing poly(vinylpyrrolidone) and sorbed water. Pharm. Res. 25, 647–656.

Marsac, P.J., Li, T., Taylor, L.S., 2009. Estimation of drug–polymer miscibility and solubility in amorphous solid dispersions using experimentally determined interaction parameters. Pharm. Res. 26, 139–151.

Marsac, P.J., Rumondor, A.C., Nivens, D.E., Kestur, U.S., Stanciu, L., Taylor, L.S., 2010. Effect of temperature and moisture on the miscibility of amorphous dispersions of felodipine and poly(vinyl pyrrolidone). J. Pharm. Sci. 99, 169–185.

Matsumoto, T., Zografi, G., 1999. Physical properties of solid molecular dispersions of indomethacin with poly(vinylpyrrolidone) and poly(vinylpyrrolidone-co-vinylacetate) in relation to indomethacin crystallization. Pharm. Res. 16, 1722–1728.

Miyazaki, T., Yoshioka, S., Aso, Y., Kojima, S., 2004. Ability of polyvinylpyrrolidone and polyacrylic acid to inhibit the crystallization of amorphous acetaminophen. J. Pharm. Sci. 93, 2710–2717.

Miyazaki, T., Yoshioka, S., Aso, Y., 2006. Physical stability of amorphous acetanilide derivatives improved by polymer excipients. Chem. Pharm. Bull. 54, 1207–1210.

Miyazaki, T., Yoshioka, S., Aso, Y., Kawanishi, T., 2007. Crystallization rate of amorphous nifedipine analogues unrelated to the glass transition temperature. Int. J. Pharm. 336, 191–195.

Rumondor, A.C., Marsac, P.J., Stanford, L.A., Taylor, L.S., 2009a. Phase behavior of poly(vinylpyrrolidone) containing amorphous solid dispersions in the presence of moisture. Mol. Pharm. 6, 1492–1505.

Rumondor, A.C.F., Ivanisevic, I., Bates, S., Alonzo, D.E., Taylor, L.S., 2009b. Evaluation of drug–polymer miscibility in amorphous solid dispersion systems. Pharm. Res. 26, 2523–2534.

Suzuki, H., Sunada, H., 1998. Influence of water-soluble polymers on the dissolution of nifedipine solid dispersions with combined carriers. Chem. Pharm. Bull. 46, 482–487.

Tanno, F., Nishiyama, Y., Kokubo, H., Obara, S., 2004. Evaluation of hypromellose acetate succinate (HPMCAS) as a carrier in solid dispersions. Drug Dev. Ind. Pharm. 30, 9–17.

Tao, J., Sun, Y., Zhang, G.G., Yu, L., 2009. Solubility of small-molecule crystals in polymers: D-mannitol in PVP, indomethacin in PVP/VA, and nifedipine in PVP/VA. Pharm. Res. 26, 855–864.

Telang, C., Mujumdar, S., Mathew, M., 2009. Improved physical stability of amorphous state through acid base interactions. J. Pharm. Sci. 98, 2149–2159.

Vippagunta, S.R., Maul, K.A., Tallavajhala, S., Grant, D.J.W., 2002. Solid-state characterization of nifedipine solid dispersions. Int. J. Pharm. 236, 111–123.

Wang, L., Cui, F.D., Hayase, T., Sunada, H., 2005. Preparation and evaluation of solid dispersion for nitrendipine–carbopol and nitrendipine–HPMCP systems using a twin screw extruder. Chem. Pharm. Bull. 53, 1240–1245.

Wang, L., Cui, F.D., Sunada, H., 2007. Improvement of the dissolution rate of nitrendipine using a new pulse combustion drying method. Chem. Pharm. Bull. 55, 1119–1125.

—Review—

ダイナミック造影磁気共鳴画像法（DCE-MRI）による微粒子製剤の腫瘍移行性評価

川野久美,* 米谷芳枝

Tumor Permeability of Nanocarriers Observed by Dynamic Contrast-enhanced Magnetic Resonance Imaging

Kumi KAWANO* and Yoshie MAITANI

Institute of Medicinal Chemistry, Hoshi University, Ebara 2-4-41, Shinagawa-ku, Tokyo 142-8501, Japan

(Received September 1, 2010)

The structure of tumor vasculature is crucial for the nanocarrier-mediated chemotherapy. Recently, transforming growth factor-β (TGF-β) inhibitor was reported to increase the tumor accumulation of nanocarriers by changing the structure of tumor vasculature. To indentify the parameters of tumor vasculature function following TGF-β inhibitor (A-83-01) treatment, dynamic contrast-enhanced magnetic resonance imaging (DCE-MRI) was performed using Gd-DTPA and its liposomal formulation (Gd-L) as contrast agents. Observation of tumor MR image before, during, and after injection of contrast agent could calculate the parameters of vascular function, such as volume transfer constant between blood plasma and extracellular space (K^{trans}) and fractional plasma volume (v_p). A-83-01 treatment significantly increased these parameters within 24 h that was positively related to pericyte coverage and tumor cell proliferation. Furthermore, apparent diffusion coefficient (ADC) determined by diffusion-weighed imaging was decreased by A-83-01 treatment, suggesting the decrease of tumor interstitial fluid pressure. Vascular function of the tumor improved by A-83-01 treatment well assessed on post-Gd-L-enhanced MR images, which predicted delivery of liposomal drug to the tumor. These findings suggest that DCE-MRI and, in particular, K^{trans} and v_p quantitation, provide important additional information about tumor vasculature by A-83-01 treatment.

Key words——liposome; tumor permeability; magnetic resonance imaging; transforming growth factor-β inhibitor

1. はじめに

がん化学療法は抗がん薬の副作用が大きく，薬物を有効濃度まで投与できないことが問題となっている．そのため，薬物を腫瘍部位へ効率よく送達することによって副作用を軽減し，治療効果を高める試みが盛んにされている．その方法の1つとして，抗がん薬を高分子化，あるいはリポソームや高分子ミセルのように微粒子化することが挙げられる．腫瘍に新生する血管は正常組織の血管に比べ血管透過性が亢進しており，数十から数百 nm スケールの微粒子においても血管外へ漏出し，また腫瘍ではリンパ管が未発達で欠如していることから高分子等の排泄が抑制されており，留まり易い．腫瘍血管はこのような特徴的な構造を持っているので，微粒子を長時間血中に滞留させると腫瘍に集積し，これは enhanced permeability and retention (EPR) 効果と呼ばれている.[1]

微粒子は低分子薬物に比べてサイズが大きいので，腫瘍の血管構造や血流の影響を受け易く，EPR 効果が十分に発揮されない場合もある．高分子では昇圧薬[2]や血管拡張薬,[3] 微粒子では，transforming growth factor-β (TGF-β) I 型受容体阻害薬[4]の併用によって腫瘍微小環境を変化させて，薬物送達性を促進する試みが報告されている．本稿では，まず TGF-β I 型受容体阻害薬である A-83-01 の腫瘍血管に対する影響をダイナミック造影磁気共鳴画像（DCE-MRI）を用いて非侵襲的に評価し，つぎに，A-83-01 処置による微粒子の透過性変化を評価したので報告する．

2. TGF-β I 型受容体阻害薬（TGF-β 阻害薬）

TGF-β の作用は多岐にわたり，細胞の増殖，分化，接着，遊走などを制御する．上皮細胞やリンパ球といった多くの細胞の増殖を抑制する代表的な増

星薬科大学医薬品化学研究所（〒142-8501 東京都品川区荏原 2-4-41）
*e-mail: kkumi@hoshi.ac.jp

本総説は，日本薬学会第 130 年会シンポジウム S10 で発表したものを中心に記述したものである．

殖抑制因子であるが，腫瘍細胞に対して上皮間葉転換，湿潤能・運動性の亢進や，がん周囲環境には免疫抑制，血管新生，細胞外基質産生を引き起こし，がん化を促進することも知られている．よって腫瘍の TGF-β シグナル阻害は，抗腫瘍効果を促進し転移の抑制効果があることが報告されているものの，逆に TGF-β の上皮細胞増殖抑制作用を減弱させて腫瘍増殖が起こるなどの副作用も考えられる．

血管は血管内皮細胞とその周囲を覆う壁細胞（血管平滑筋細胞，ペリサイト）からなり，壁細胞が裏打ちすることにより構造的に安定化し，機能を示す．腫瘍などの病的血管ではペリサイトの配列異常や欠如があり，血流の不整など血管の機能性が低い．しかし膵臓がんやびまん性の胃がんなどの難治性腫瘍ではペリサイト被覆の強い血管構築性を示し，微粒子を用いた化学療法が奏功しない．Kano らは，このような微粒子集積性の低い腫瘍に対して，TGF-β 阻害薬（LY364947）の副作用を最小にするために低用量で併用し，ドキソルビシン封入高分子ミセル又はリポソームの腫瘍集積性を向上させ，治療効果を増大させた.[4] これは TGF-β 阻害薬が腫瘍新生血管のペリサイトの被覆を一過的に減少させたためである．LY364947 の併用によりフリーのドキソルビシンの集積量は増加しなかったことから，ペリサイトの存在が特に微粒子の血管透過性に関与すると報告されている．

TGF-β I 型受容体阻害薬である A-83-01[5] は，*in vitro* で TGF-β I 型受容体キナーゼ（ALK-5）に対して IC_{50}＝12 nM の TGF-β シグナル阻害活性を有し，前出の LY364947（IC_{50}＝59 nM）に比べて約 5 倍高い阻害活性を有する．しかし，*in vivo* での腫瘍血管に対する作用はこれまで報告されていなかった．そこで，A-83-01 の腫瘍血管透過性に対する作用を MRI を用いて調べた．

3. ダイナミック造影 MRI（DCE-MRI）

筆者らは，血管透過性の評価方法としてダイナミック造影 MRI（dynamic contrast-enhanced magnetic resonance imaging, DCE-MRI）に着目した．DCE-MRI は近年盛んに開発されている血管新生阻害薬の臨床試験での評価に用いられている．血管新生阻害薬は腫瘍新生血管に作用することによりがん細胞の増殖抑制に働くために，これまでの抗がん薬のように腫瘍サイズの縮小などをエンドポイントとすると正確な評価が困難である．腫瘍内の血管変化は，腫瘍切片の免疫染色による血管分布や構造変化，あるいは蛍光物質を用いて血流の有無や血管透過性を顕微鏡観察して評価される．しかしこのような侵襲的な手法は，経時的な評価に多数の動物を必要とし，臨床での応用性に乏しいなどの欠点を有する．一方，DCE-MRI は血管の機能を非侵襲的に評価する方法であり，血管新生阻害薬が血管透過性に影響する初期の薬効，すなわち，効果が腫瘍サイズに反映する前に評価することが可能となる.[6]

DCE-MRI 法では，連続的に腫瘍の撮像を行いながら MRI 造影剤の投与を行う．腫瘍内の信号強度変化は血流による造影剤の移行量に相当し，血流量，血管の表面積や透過性，血管外細胞外の体積（v_e）などが関与する（Fig. 1）．よって腫瘍画像強度変化を解析することで，造影剤の移行性に係わるこれらの変化を表すパラメータを得ることができる．

以下に DCE-MRI による評価に用いられるパラメータについて説明する．MRI 造影剤ではシグナル強度と濃度に単純な比例関係がないため濃度を算出するのは困難なものの，定量性の高い撮像シーク

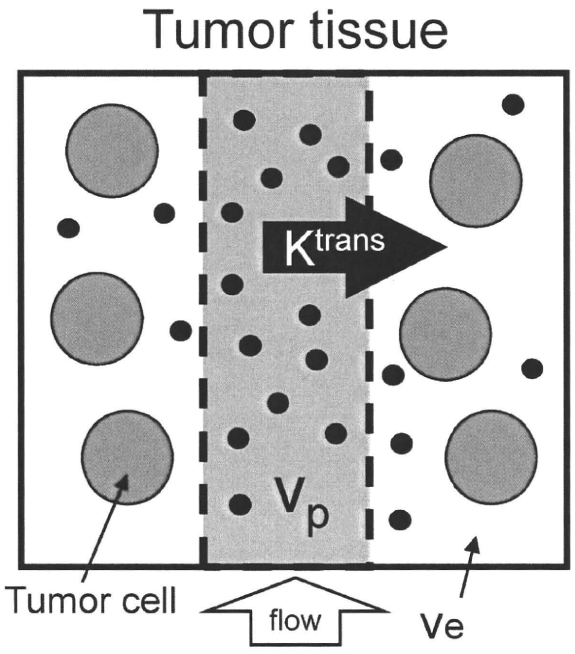

Fig. 1. Compartmental Modeling of the Tumor Microvasculature

Contrast agents (represented as black dots) distribute in the blood plasma volume (v_p) and the volume of the extravascular extracellular space (v_e). The rate of transfer is described by the volume transfer constant (K^{trans}) from blood plasma to the v_e.

エンスを選択することで薬動学的に解析することが可能となる．造影剤投与直後の腫瘍内造影剤濃度-時間曲線下面積 initial area under the contrast agent concentration-time curve (IAUGC) は比較的求め易いパラメータであるが，どのような生理的現象の変化によって透過性が変化したのかを深く言及できない．そこで，さらに生理的な変化を解析するために薬動学的モデル解析が行われる．[7] 組織中の造影剤濃度（C_t）は，血漿中濃度（C_p）と組織（v_e）に分布した量の和として考えられ，コンパートメントモデルに当てはめて解析すると Eq. (1) が得られる．[8]

$$C_t(t) = K^{trans} \int_0^t C_p(\tau)\, d\tau + v_p C_p(t) \qquad (1)$$

ここで，K^{trans} は血液から組織への移行定数であり，v_p は腫瘍内血漿体積である．両辺を $C_p(t)$ で除して得られる直線からこれらのパラメータは算出することができ，パトラックプロットと呼ばれる．[9] K^{trans} は血管透過性のパラメータとして用いられるが，このように単純化したモデルから求められる K^{trans} は純粋な血管透過性のみではなく，血流や血管の表面積などにも影響される．より詳細なコンパートメントモデルを想定することでこれらの因子を区別することも可能であるが，[7] より高い時間分解能が必要とされ実現には困難を伴うため，想定したモデルに応じたパラメータの解釈が必要とされる．血管新生阻害薬や血流遮断薬の評価には，IAUGC や K^{trans} が基本的なバイオマーカーとして用いられている．[10]

4. 微粒子造影剤を用いた DCE-MRI による TGF-β 阻害薬の評価

TGF-β 阻害薬 A-83-01 の腫瘍血管透過性に対する作用を評価するために，マウス結腸がん colon26 細胞皮下移植マウスで DCE-MRI を行った．なお以後の実験は，星薬科大学の動物実験委員会に諮られ承認を受けたものである．MRI 装置は 9.4 T 垂直型 MRI（Varian NMR System; Varian, Inc.）を使用した．

DCE-MRI に用いる造影剤としては，常磁性の Gd イオンをキレート化した Gd-DTPA や Gd-DOTA などの低分子造影剤が臨床で使用されている．Gd イオンは周囲のプロトンに作用し水分子の T_1 緩和時間を短縮することから，T_1 強調画像で画像強度を増強する陽性造影剤である．DCE-MRI において従来の低分子造影剤を用いると，血流の影響が大きく血管透過性を正確に見積もることが難しい．そこで，血管透過を律速にして血流の影響を無視できるようにするために，アルブミンのような高分子化した造影剤が使用されるようになっている．[11,12] ここではさらにサイズの大きい Gd-DTPA 封入リポソーム（Gd-L）を造影剤として用いることで，血管透過性の評価に加えて微粒子製剤の腫瘍移行性を調べることにした．

Gd-L は，卵黄フォスファチジルコリン，コレステロール，PEG_{2000}-DSPE からなるリポソームに Gd-DTPA を内封し，粒子径を約 120 nm に調整した．T_1 強調画像の信号強度を高める能力である T_1 緩和能は，4.5 $mM^{-1}\,s^{-1}$ であり，フリーの Gd-DTPA（4.4 $mM^{-1}\,s^{-1}$）と同程度であることを確認した．DCE-MRI における撮像は，T_1 強調スポイルドグラジエントエコー法により 1 秒間に 1 枚ずつ 6 分間行った．時間分解能を高めることで造影剤投与時における血液の画像強度増加の正確なピークの取得を可能とし，カーブフィッティングや血行動態の解析精度を高めることが可能である．腫瘍と左心室を含むスライスを設定し，ベースラインを約 20 秒間取得したのち，造影剤（0.1 mmol Gd/kg）を投与した．

A-83-01 投与と DCE-MRI の実施は Fig. 2 (A) に示すスケジュールで行い，各時間での腫瘍内 Gd 濃度推移を Fig. 2（B, C）に示す．低分子の Gd-DTPA を用いると，A-83-01 を腹腔内投与 3 時間後において腫瘍内 Gd 濃度が高くなったが，投与 24 時間後には投与前と同程度に戻った［Fig. 2 (B)］．すなわち A-83-01 の効果は一過的であると考えられる．また，投与 3 時間後では個体間で移行性にばらつきが認められたが，A-83-01 を 21 時間目に追加投与した繰り返し投与（A-83-01×2）では，すべてのマウスにおいて Gd 濃度が増大した．そこで，繰り返し投与時の微粒子の移行性を Gd-L を用いて評価した［Fig. 2 (C)］．未処置の腫瘍では，Gd-L は Gd-DTPA を用いたときに比べて，低い腫瘍内 Gd 濃度を示した．これは Gd-L は微粒子であるために，低分子に比べ腫瘍への移行性が低下したと考えられる．しかし，A-83-01 を繰り返し投与すると Gd-DTPA を用いたときと同様に高い腫瘍内 Gd 濃度を示した．この得られた腫瘍内 Gd 濃度-時間